Stability Region Estimation of Grid-Forming IBRs with Direct Current Limiters via Energy Function

Mohammad Ali Dashtaki and Ziang Zhang
Binghamton University - SUNY
Binghamton, NY, USA
mdashta1@binghamton.edu,
ziang.zhang@binghamton.edu

Debjyoti Chatterjee and Brian Johnson
University of Texas at Austin
Austin, TX, USA
debjyotichatterjee@utexas.edu,
b.johnson@utexas.edu

Hsiao-Dong Chiang
Cornell University
Ithaca, NY, USA
chiang@ece.cornell.edu

***Abstract*— Current limiters are embedded within grid-forming (GFM) controllers to protect inverter-based resources (IBRs) from post-fault overcurrents. For direct current limiters based on current-reference saturation, the saturated current angle (SCA) strongly influences the transient stability of GFM inverters. This paper presents a novel energy-function-based framework for assessing the transient stability region of GFM IBRs equipped with direct current limiters. Using the derived energy function, the stable and unstable equilibrium points are analytically identified. Also, the proposed energy function captures the effect of the SCA on post-fault dynamics and enables quantitative characterization of the stability region under varying SCA values. The analysis demonstrates that an optimally selected SCA enlarges the stability region and ensures a smooth transition from current-source to voltage-source operation once the fault is cleared. Theoretical findings are validated through detailed time-domain simulations.**

Keywords—transient stability analysis, grid-forming inverters, current limiter, energy function, direct method

I. Introduction

Grid-forming (GFM) control has emerged as a key strategy for integrating inverter-based resources into modern power systems [1]. Among different grid-forming implementations, the virtual synchronous machine (VSM) approach is one of the most widely adopted [2]. However, because GFM inverters use power-electronic switches with strict thermal limits, an effective current-limiting mechanism is essential to protect them during fault conditions [3]. Unlike SGs, which can withstand short-term overcurrents several times their rated value, GFM inverters are typically limited to about 1.2 p.u. of rated current [4]. Ensuring that an inverter can ride through grid faults without exceeding its current limits and maintaining synchronization with the grid is therefore of paramount importance [5].

To address this need, several current-limiting techniques have been proposed for GFM inverters. The virtual-impedance (VI) method, an indirect current-limiting approach, and direct current-limiting (DCL) strategies based on current-reference saturation are the two main categories explored in recent literature [6]. The DCL approach is particularly effective during the initial fault period, providing fast and accurate current limitation [7]. Nevertheless, because this method requires the inverter to temporarily switch to current-source mode (CSM) during overcurrent conditions, it may adversely affect transient synchronization stability [8]. Consequently, a comprehensive analysis of the transient stability of GFM inverters equipped with DCLs is necessary.

The saturated current angle (SCA) in the direct current-limiting method significantly affects the transient stability of GFM IBRs. Furthermore, the SCA value should be selected to ensure that the GFM IBR switches back to normal GFM operation (as a VSC) post-fault when the current value is below its threshold. In [9], the Lyapunov energy function is used to analyze the transient stability of the GFMs when the current limiter is in effect after the fault. Moreover, the phase portrait and stability region of the system under different SCA values are depicted. However, it is assumed that the inverter will remain in the CSM after the fault. The inverter should be able to switch to the GFM mode under every SCA value to guarantee continuous frequency and voltage regulation after the fault is cleared. In [10], the stability region under the current saturated mode is obtained, and the SCA is designed accordingly. Nonetheless, similar to [9], the inverter operates as a current source post-fault. In another effort, an optimal SCA value that guarantees a smooth switch from CSM to VSC after a fault is introduced in [11]. Nevertheless, it lacks a comprehensive transient stability analysis that spans a range of SCAs and maps the resulting stability region.

The existing studies on energy functions primarily examine inverters with virtual-impedance-based current limiters, without addressing inverter mode switching when the current limit is reached [6]. As more inverters employ direct current limiters that require a mode change, this paper investigates transient stability in a full hybrid dynamical sequence induced by mode transition.

Therefore, this paper addresses the research gap by conducting a comprehensive analysis of how the saturated current angle affects the transient stability of GFM inverters while ensuring proper switching between current-source and grid-forming modes. To quantitatively determine the stability margin without relying on extensive time-domain simulations, an energy-function-based analytical framework is developed. The main contributions of this work are:

- As a first attempt, an energy function is derived for the GFM inverter system that explicitly accounts for the impacts of the direct current limiter. Moreover, the proposed energy function is applicable to handle similar hybrid dynamical systems that switch modes during operation.
- The effect of the saturated current angle on the estimated stability boundary of the power system is demonstrated using the newly proposed energy function. The accuracy of the proposed method is validated through brute-force time-domain simulations.

The rest of the paper is structured as follows. In Section II, the model explanation and potential energy calculation are performed. The simulation results under different SCA values are provided in Section III. The conclusion of the paper is expressed in Section IV.

II. Model Explanation

In this section, the mathematical formulation of a single-inverter infinite bus (SIIB) system is presented. Then, the direct current limiting mechanism is described. Next, the potential energy formulation is derived, and the candidate

XXX-X-XXXX-XXXX-X/XX/$XX.00 ©20XX IEEE
979-8-3315-8138-1

total energy is verified to be an energy function. Finally, the SCA range is determined to ensure a seamless transition back from CSM to GFM mode. The equations presented in this section will be applied to estimate the stability region.

A. SIIB System Explanation

In this paper, the VSM-based IBR unit is modeled as a controllable voltage source in series with an impedance in the phasor domain. As shown in Fig. 1, the IBR terminal voltage and current phasor are shown as $E\angle\delta$ and $I\angle\varphi$, respectively. The infinite bus voltage phasor, IBR reactance, grid reactance, and total reactance are $V_g\angle 0$, X_{IBR}, X_g, X_t, respectively. Moreover, P, Q, P_{ref} and Q_{ref} are the measured active and reactive power, and reference active and reactive power, respectively. The dynamical equations of the SIIB system are similar to a classic swing equation written as below [12]:

$$P_{ref} - P_e(\delta) = M\frac{d\omega}{dt} + D\omega, \tag{1}$$

$$\omega = \frac{d\delta}{dt}, \tag{2}$$

where M is the virtual inertia, and D is the virtual damping. For notational simplicity, we write the dynamic states as δ and ω instead of $\delta(t)$ and $\omega(t)$. Thus, δ and ω are always representing the time-varying states unless explicitly labeled as a constant, such as the switching angle δ_{sw}.

B. Current Limiting Mechanism

The direct current limiting approach, which is the common method used to limit the inverter's overcurrent [6], is expressed in this section. In this strategy, the GFM IBR operates as a conventional voltage-source inverter when the current is not saturated. However, when the current magnitude exceeds the maximum allowed current limit, I_{max}, the GFM inverter will act as a constant current source. The current magnitude can be represented as a function of δ:

$$|I| = \frac{|E\angle\delta - V_g\angle 0|}{X_g} = \frac{1}{X_g}\sqrt{E^2 + V_g{}^2 - 2EV_g\cos\delta}. \tag{3}$$

Thus, the switching δ values, where the GFM IBR mode changes to the CSM and $|I| = I_{max}$, can be found as below:

$$\delta_{sw} = \pm\arccos\left(\frac{E^2 + V_g^2 - (X_g I_{max})^2}{2EV_g}\right) + 2\pi k. \quad k \in Z \tag{4}$$

The output active power of the inverter under VSC and CSM modes can be expressed as follows [6]:

$$P_e(\delta) = \begin{cases} \frac{EV_g}{X_g}\sin\delta = P_{max}\sin\delta, & if\ |\delta| < |\delta_{sw}| \\ V_g I_{max}\cos(\delta - \varphi), & if\ |\delta| > |\delta_{sw}| \end{cases} \tag{5}$$

where φ is the saturated current angle, which is an adjustable variable when the direct current limiter is in effect. Note that φ is measured in the local reference frame defined by the angle of the primary controller. It is worth mentioning that according to equation (4), changing the φ parameter will not affect the switching δ value. As mentioned in the previous section, in this paper, the effect of φ (or SCA) on the transient stability of the GFM inverter will be investigated. Equations (1)-(5) are a hybrid dynamical system used to model the SIIB system with a current limiter.

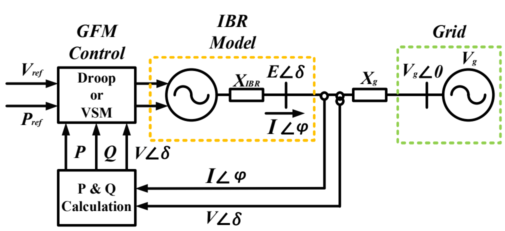

Fig. 1. Phasor-domain model of a GFM.

C. The Energy Function of an IBR with Current Limiter

The potential energy $U(\delta)$ and total energy $V(\omega,\delta)$ of the system above, can be expressed as below:

$$U(\delta) = -\int_{\delta_s}^{\delta}\left(P_{ref} - P_e(\delta)\right), \tag{6}$$

$$V(\omega,\delta) = U(\delta) + \frac{1}{2}M\omega^2. \tag{7}$$

The potential energy of a VSM-based IBR without a current limiter can be written as follows ([13] and [14]):

$$U(\delta) = -P_{ref}(\delta - \delta_s) - P_{max}(\cos\delta - \cos\delta_s), \tag{8}$$

where δ_s is the inverter's relative voltage angle with respect to the infinite bus, when $P_{ref} = P_e(\delta)$ or in other words, the δ value at the SEP. In our system under study, although $P_e(\delta)$ is written piecewise, both branches are bounded functions of δ. Hence, the integrand will be bounded and integrable. According to the fundamental theorem of calculus (Lebesgue version), $U(\delta)$ is absolutely continuous, and cannot have a jump. A jump would require a Dirac impulse in U', which our model does not have. When δ crosses the limit engagement point δ_{sw}, the potential energy can be calculated as:

$$U(\delta) = \underbrace{-\int_{\delta_s}^{\delta_{sw}}\left(P_{ref} - \frac{EV_g}{X_g}\sin\delta\right)d\delta}_{Unconstrained\ (VSC\ mode)} \underbrace{-\int_{\delta_{sw}}^{\delta}\left(P_{ref} - V_g I_{max}\cos(\delta - \varphi)\right)d\delta}_{Constrained\ (CSM)}. \tag{9}$$

Hence, $U(\delta)$ will be continuous around δ_{sw}. According to equation (9), $U(\delta)$ can be calculated as below

$$U(\delta) = -P_{ref}(\delta - \delta_s) + VI_{max}\sin(\delta - \varphi) + C_0, \tag{10}$$

where $C_0 = -P_{max}(\cos\delta_{sw} - \cos\delta_s) - P_{ref}(\delta_{sw} - \delta_s) - VI_{max}\sin(\delta_{sw} - \delta_s)$, is a constant and does not depend on δ. If the δ value is less than δ_{sw}, only the unconstrained part of the potential energy formula should be calculated. The energy function proof of the above equations is delivered in the Appendix section.

D. SCA range for the GFM IBR system

As described in the reference [11], during a post-fault situation, to guarantee the IBR will switch back from the CSM to the GFM mode, the SCA value should meet the following condition

$$\varphi \le \arcsin\left(\frac{P_{ref}}{P_{max}}\right) + \arccos\left(\frac{P_{ref}}{V_g I_{max}}\right). \tag{11}$$

III. Simulation Results

In this section, first, the baseline case without current limiters is analyzed, and the stability boundary of the system, along with sample trajectories, is derived. Note that a wide range of δ values is chosen to determine the stability region of the system under both VSC mode and CSM. Next, the validity of the approximated stability boundary is proved using a Brute-Force approach. Subsequently, the same investigation is conducted in the next subsections, while the

979-8-3315-8138-1

TABLE I. SYSTEM AND CONTROLLER PARAMETERS.

Parameter	Value (p.u.)
Reference active power (P_{ref})	0.7
IBR terminal voltage magnitude (E)	1.0
Infinite bus voltage magnitude (V_g)	1.0
Virtual inertia coefficient (M)	2.0
Virtual damping coefficient (D)	0.35
Maximum allowed current limit (I_{max})	1.2

φ value increases from zero to the upper bound of SCA in equation (21), called φ^*. The system and controller parameters are summarized in Table 1. In this case, $P_{max} = 1.25$, $V_g I_{max} = 1.2$, and $\varphi^* = 89°$.

A. Baseline Case

The baseline case, where no current limiters are considered for the SIIB system, is analyzed in this section. The potential energy U and its first derivative, U', the second derivative, U'', and the current magnitude are shown in Fig. 2. The UEP and SEP are shown as red and green dots, respectively. As observed from the U' plot, the points at which the first derivative of the potential energy becomes zero, correspond to the system's equilibrium points. As shown, the first equilibrium point is an SEP, as the U''>0 at this point. On the contrary, the second equilibrium point in each period is a type-one UEP, since the U'' <0.

The phase portrait of the system and its stability boundary are shown in Fig. 3. Additionally, the time-domain simulation of the system is performed with two different initialization parameters to illustrate stable and unstable trajectory cases. Note that the total energy contour is illustrated in different colors to show the energy level. It is worth noting that when a fault occurs, the system's states will drift away from the SEP. Once the fault is cleared, the post-fault initial condition is what is shown as the starting point in the phase portrait diagram. One benefit of the energy-function-based approach is that it is not limited to a single fault condition.

B. Stability Boundary when $\varphi = 0$

The stability impact of the direct current limiter and the potential energy of the SIIB system, assuming $\varphi = 0$ is analyzed in this section. The potential energy, U', U'', and the current magnitude are shown in Fig. 4. As depicted, exactly at the red point, the U'' curve changes its sign from positive to negative. Accordingly, before and after the red point, the time-domain trajectories become stable and unstable, respectively. Hence, the red point should be located on the stability boundary and be considered as a UEP. It is worth noting that the UEP plays a crucial role in determining the stability region of the system under study, as its energy is the critical energy of the SIIB. Meaning that if the initial energy of the system is less than this energy, the system will remain stable. Otherwise, the system will face instability. The points at which the inverter current magnitude exceeds the maximum rated current, referred to as the switching angles, δ_{sw}, are illustrated in Fig. 4. Note that in our case, whenever the DCL strategy is used, $\delta_{sw} \approx \pm 1.0013$ rad.

The phase portrait and stability boundary of the SIIB system with the direct current limiter when $\varphi = 0$ are shown in Fig. 5. Different time-domain trajectories according to the dynamics of the system are considered to evaluate the validity of the stability boundary. As can be seen, when the initialization parameters (ω_0, δ_0) are slightly out of the stability boundary, the trajectory will become unstable. To further evaluate the accuracy of the stability boundary found, the Brute-Force approach is utilized in Fig. 6, and 810,000 time-domain simulations are performed. The green and yellow dots indicate the initialization conditions (ICs) for stable and unstable trajectories, respectively. Note that the simulation step size (T_{step}) is around 0.002, $\delta_0 \in [-1.5, 3]$ rad, and $\omega_0 \in [-1, 1]$ rad/s. The simulation time for each initialization condition (T_{span}) is 30s. As can be seen, the

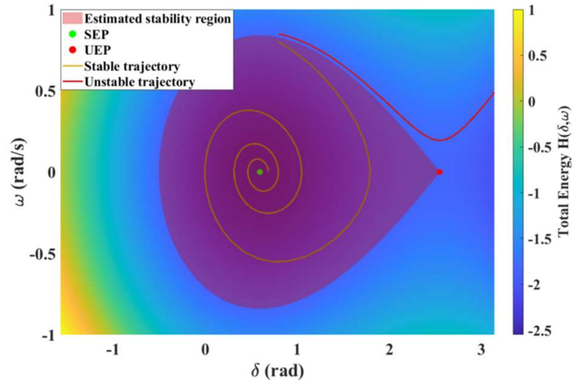

Fig. 3. Phase portrait with stability boundary and sample trajectories (no current limiter).

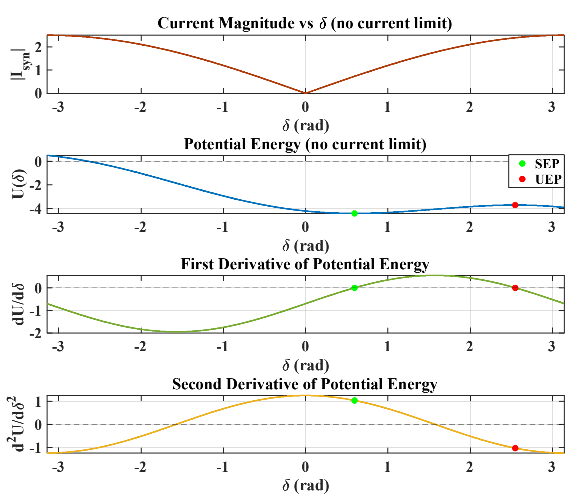

Fig. 2. Potential energy, its first and second derivatives, and current magnitude of the SIIB system when the current limiter is not embedded.

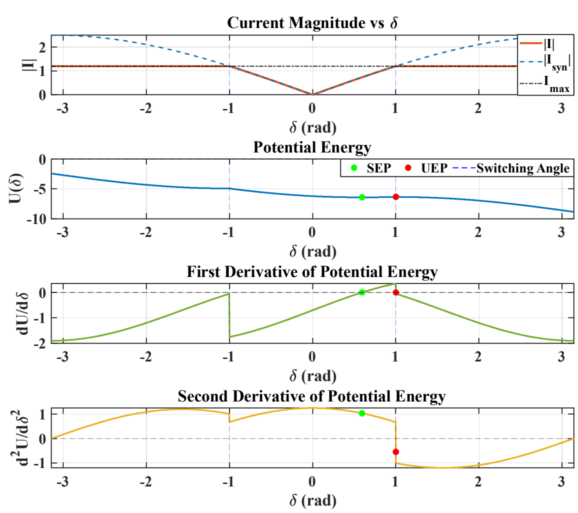

Fig. 4. Potential energy, its first and second derivatives, and current magnitude when $\varphi = 0$.

979-8-3315-8138-1

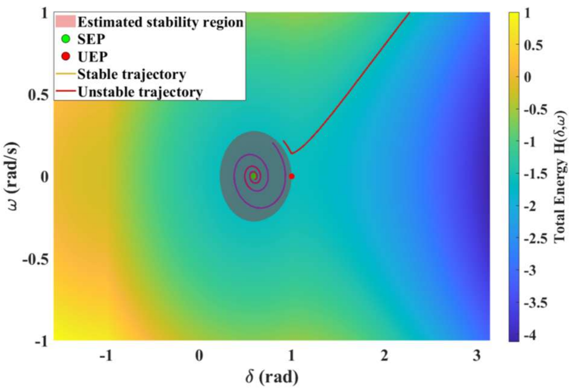

Fig. 5. Phase portrait with stability region and stable and unstable trajectories when $\varphi = 0$.

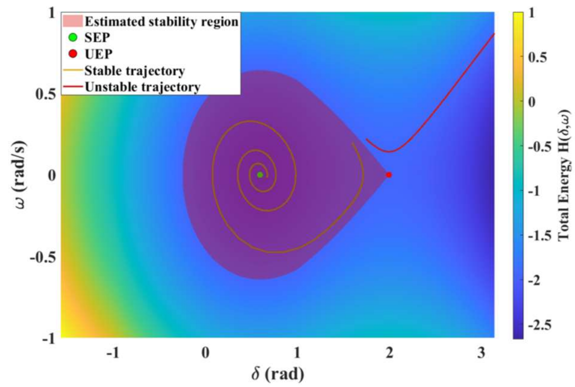

Fig. 7. Phase portrait with stability region and stable and unstable trajectories when $\varphi = \pi/3$.

stability boundary found by the Brute-Force method is in line with the stability boundary shown in Fig. 5, which validates our methodology in estimating the SIIB stability boundary when the current limiter is considered and $\varphi = 0$. By comparing Fig. 3 and Fig. 5, it can be concluded that when $\varphi = 0$, by applying the direct current limiter in the GFM IBR controller, the stability boundary of the system will shrink.

C. Stability Boundary when $\varphi = \pi/3$

The transient stability of the SIIB system with the direct current limiter when φ is increased from zero to $\pi/3$ is investigated in this section. Fig. 7 shows the stability boundary of the system on a phase portrait. Two sample trajectories are considered to show the validity of the estimated stability boundary. By comparing Fig. 5 and Fig. 7, it can be concluded that by increasing the φ value from zero to $\pi/3$, the stability region of the SIIB system has enlarged. Note that the switching angles δ_{sw} and SEP location will remain unchanged. However, the UEP location will be shifted by φ, resulting in a change in the UEP potential energy and the system's critical energy. Similar to the previous case, to further assess the accuracy of the realized stability region, 810,000 time-domain simulations were conducted. As shown in Fig. 8, the stability region obtained using the Brute-Force approach aligns with the results presented in Fig. 7.

D. Comparing the Stability Boundary with different φ

This section summarizes the key findings of the previous analyses. In Fig. 9, on the same phase portrait, the stability regions of the system under different φ values are shown. As φ increases, the SEP remains unchanged, whereas UEP shifts toward the right along the δ-axis. Consequently, as the UEP moves and the associated critical energy increases, the overall stability region monotonically expands. Therefore, φ should be chosen as large as possible while satisfying the recoverability condition in (11) to ensure smooth return to grid-forming operation. This condition provides a simple offline tuning rule based on the power reference and current limit. While parameter uncertainties affect the switching angle and absolute stability margin, the stabilizing effect of increasing φ remains qualitatively unchanged. Accordingly, although introducing the DCL strategy in the GFM controller reduces the stability region, selecting an appropriate SCA value can maximize system stability.

IV. Conclusion

Despite prior SCA-oriented energy function studies, where only the CSM is considered as the post-fault operating condition, this paper fully studies hybrid operational modes under the direct current limiter effect. Furthermore, this paper presents an energy-function-based method for assessing the transient stability of GFM inverters with current limiters. By incorporating the current limiter into the energy function formulation, the stable and unstable equilibrium points, along with their corresponding stability regions, were analytically identified. The proposed energy function can be used to estimate stability in hybrid dynamical systems. The results showed that the current limiter strongly influences post-fault stability: increasing the SCA shifts the UEP and enlarges the stability region. Proper selection of SCA enables smooth recovery from current-source to grid-forming operation. The analytical stability boundaries were validated through extensive time-domain simulations, confirming the accuracy of the proposed method. Since the SIIB system does not capture the DCL-induced nonlinearity among parallel

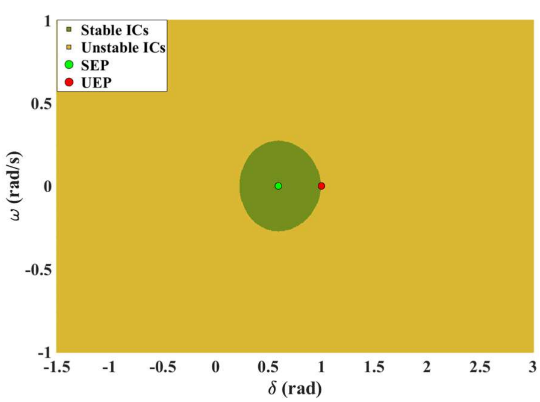

Fig. 6. Brute-Force stability boundary when $\varphi = 0$.

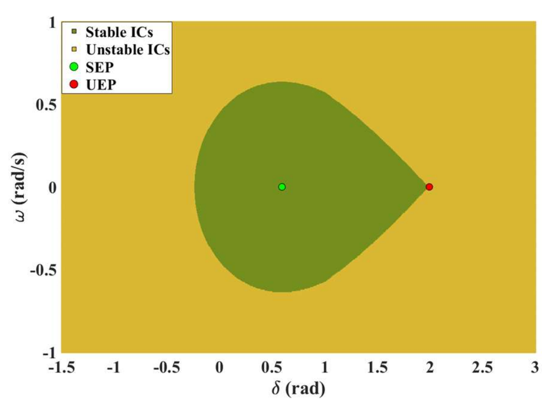

Fig. 8. Brute-Force stability boundary when $\varphi = \pi/3$.

979-8-3315-8138-1

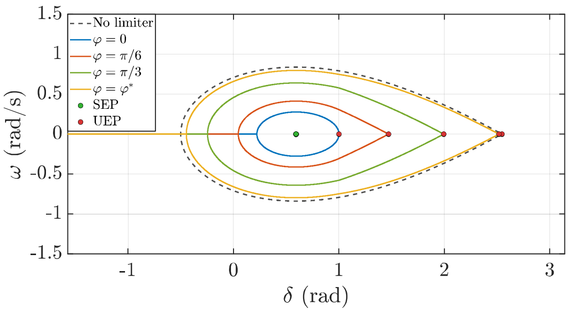

Fig. 9. Estimated stability region under different φ.

inverters, future work will extend the proposed framework to multi-inverter and more complex configurations.

Appendix

Using the equations in Section II, we verify the three standard conditions of an energy function [12] as follows.

1) Dissipation Inequality

Differentiating (7) along the trajectories of (1) and (2) gives

$$\dot{V} = U'(\delta)\dot{\delta} + M\omega\dot{\omega} = \left(P_e(\delta) - P_{ref}\right)\omega + \omega(P_{ref} - P_e(\delta) - D\omega = -D\omega^2 \leq 0. \quad (12)$$

Thus, V is non-increasing along all trajectories. This condition holds in both operating regions since equation (12) is valid under all operational conditions.

2) Nontrivial trajectories do not stall in energy:

Suppose $\dot{V} = 0$ over a time interval of nonzero length. From (12), this implies $\omega \equiv 0$ on this interval. Substituting $\omega = 0$ into (1) and (2) yields $P_{ref} - P_e(\delta) = 0$. Therefore, δ must satisfy the equilibrium condition. Hence, the only trajectories on which V remains constant over a nontrivial time interval are equilibria. This verifies Condition 2.

3) Boundedness Condition (Dynamic Properness)

By integrating equation (1) for $\omega(t)$, we will have:

$$\omega(t) = e^{-\frac{D}{M}t}\left[\omega_0 + \frac{1}{M}\int_b^a e^{\frac{D}{M}\tau}\underbrace{\left(P_{ref} - P_e\big(\delta(\tau)\big)\right)}_{x} d\tau\right], (13)$$

where on each interval $[a, b]$ we pick $P_e = P_{max}\sin\delta$, or $P_e = V_g I_{max}\cos(\delta - \varphi)$ depending on the operation mode. since I_{max}, and P_{ref} are constant values, the term noted as "x" is uniformly bounded by, for instance, a constant C_1:

$$\left|P_{ref} - V_g I_{max}\cos(\delta - \varphi)\right| \leq C_1. \quad (14)$$

In our system, D and M are positive. Thus, according to equation (14), $|\omega(t)|$ is bounded as below:

$$|\omega(t)| \leq |\omega_0| + C_1\frac{M}{D}. \quad (15)$$

Therefore, we showed that $\omega(t)$ is bounded by $C_2 = |\omega_0| + C_1\frac{M}{D}$. To prove that condition 3 is satisfied, assume $C_3 < V(\omega, \delta) < C_4$. As a result, we will have:

$$C_3 - \frac{1}{2}M\omega^2 < \underbrace{-\frac{EV_g}{X_g}(\cos\delta_{sw} - \cos\delta_s) - P_{ref}(\delta_{sw} - \delta_s)}_{y} + \underbrace{V_g I_{max}(\sin(\delta - \varphi) - \sin(\delta_{sw} - \varphi))}_{z} - P_{ref}(\delta - \delta_{sw}) < C_4 - \frac{1}{2}M\omega^2, \quad (16)$$

Since δ_{sw}, δ_s, E, V_g, X_g are constant values, the term noted by "y" is bounded by C_5. Moreover, the term "z" is uniformly bounded by C_6. Also, the term $P_{ref}\delta_{sw}$ is a constant value. Hence, by substituting C_5 and C_6, equation (16) can be rewritten as:

$$C_3 - \frac{1}{2}M\omega^2 - C_5 - C_6 - P_{ref}\delta_{sw} < -P_{ref}\delta < C_4 - \frac{1}{2}M\omega^2 + C_5 + C_6 - P_{ref}\delta_{sw}. \quad (17)$$

Therefore, the term $\delta(t)$ is bounded. Along with the result derived from equation (15), it can be concluded that the trajectory $V(\omega, \delta)$ is bounded on the stability boundary. Thus, condition 3 is satisfied [12]. Hence, the function in equation (7) is an energy function of the proposed hybrid dynamical system (1)-(5).

References

[1] Y. Lin *et al.*, "Research Roadmap on Grid-Forming Inverters," Golden, CO (United States), Nov. 2020.

[2] N. Baeckeland, D. Pal, G.-S. Seo, B. Johnson, and S. Dhople, "Large-Signal Stability Analysis of Grid-Forming Inverters With Equivalent-Circuit Models," *IEEE Transactions on Energy Conversion*, vol. 40, no. 3, pp. 2453–2465, 2025.

[3] Y. Zhang, C. Zhang, R. Yang, M. Molinas, and X. Cai, "Current-Constrained Power-Angle Characterization Method for Transient Stability Analysis of Grid-Forming Voltage Source Converters," *IEEE Transactions on Energy Conversion*, vol. 38, no. 2, 2023.

[4] G. Denis, T. Prevost, M. S. Debry, F. Xavier, X. Guillaud, and A. Menze, "The migrate project: The challenges of operating a transmission grid with only inverter-based generation. A grid-forming control improvement with transient current-limiting control," in *IET Renewable Power Generation*, 2018.

[5] M. A. Dashtaki, X. Lin, Z. Zhang, R. Pourramezan, S. Basumallik, and H. Hooshyar, "Transient Stability Enhancement via Grid-Forming IBRs on a 5000-bus New York Transmission System," in *2025 IEEE Power & Energy Society General Meeting (PESGM)*, Austin, TX, 2025.

[6] N. Baeckeland, D. Chatterjee, M. Lu, B. Johnson, and G.-S. Seo, "Overcurrent Limiting in Grid-Forming Inverters: A Comprehensive Review and Discussion," *IEEE Trans Power Electron*, vol. 39, no. 11, pp. 14493–14517, 2024.

[7] I. Sadeghkhani, M. E. H. Golshan, J. M. Guerrero, and A. Mehrizi-Sani, "A Current Limiting Strategy to Improve Fault Ride-Through of Inverter Interfaced Autonomous Microgrids," *IEEE Trans Smart Grid*, vol. 8, no. 5, 2017.

[8] L. Huang, H. Xin, Z. Wang, L. Zhang, K. Wu, and J. Hu, "Transient Stability Analysis and Control Design of Droop-Controlled Voltage Source Converters Considering Current Limitation," *IEEE Trans Smart Grid*, vol. 10, no. 1, 2019.

[9] Y. Liu, H. Geng, M. Huang, and X. Zha, "Dynamic current limiting of grid-forming converters for transient synchronization stability enhancement," *IEEE Trans Ind Appl*, vol. 60, no. 2, 2023.

[10] C. Luo, Y. Chen, S. Liao, Z. Wang, Z. Xie, and Z. Lian, "Design-Oriented Analysis and Transient Control for VSG With Current Saturation Unit," *IEEE Trans Power Electron*, vol. 40, no. 1, pp. 2472–2483, 2025.

[11] E. Rokrok, T. Qoria, A. Bruyere, B. Francois, and X. Guillaud, "Transient Stability Assessment and Enhancement of Grid-Forming Converters Embedding Current Reference Saturation as Current Limiting Strategy," *IEEE Trans on Power Systems*, vol. 37, no. 2, 2022.

[12] H. D. Chiang, *Direct Methods for Stability Analysis of Electric Power Systems: Theoretical Foundation, BCU Methodologies, and Applications*. 2010.

[13] X. Fu *et al.*, "Large-Signal Stability of Grid-Forming and Grid-Following Controls in Voltage Source Converter: A Comparative Study," *IEEE Trans Power Electron*, vol. 36, no. 7, 2021.

[14] Xuheng Lin and Ziang Zhang, "Stability Region Assessment of Power Systems with Mixed IBRs and Generators via Energy Function," in *51th Annual Conference of the IEEE Industrial Electronics Society (IECON 2025)*, Madrid, Spain, 2025.

979-8-3315-8138-1